Sathyan, Sabin; Belahcen, Anouar; Lehikoinen, Antti; Aydin, Ugur; Boxberg, Fredrik

Investigation of the causes behind the vibrations of a high-speed solid-rotor induction motor

Published in:
Journal of Sound and Vibration

DOI:
10.1016/j.jsv.2019.114976

Published: 22/12/2019

Document Version
Peer-reviewed accepted author manuscript, also known as Final accepted manuscript or Post-print

Please cite the original version:
Sathyan, S., Belahcen, A., Lehikoinen, A., Aydin, U., & Boxberg, F. (2019). Investigation of the causes behind the vibrations of a high-speed solid-rotor induction motor. *Journal of Sound and Vibration*, *463*, Article 114976. https://doi.org/10.1016/j.jsv.2019.114976

Journal Pre-proof

Investigation of the causes behind the vibrations of a high-speed solid-rotor induction motor

Sabin Sathyan, Anouar Belahcen, Antti Lehikoinen, Ugur Aydin, Fredrik Boxberg

PII: S0022-460X(19)30538-3

DOI: https://doi.org/10.1016/j.jsv.2019.114976

Reference: YJSVI 114976

To appear in: *Journal of Sound and Vibration*

Received Date: 22 May 2019

Revised Date: 18 September 2019

Accepted Date: 19 September 2019

JOURNAL OF SOUND AND VIBRATION

Available online at www.sciencedirect.com

Journal of Sound and Vibration

Journal homepage: www.elsevier.com/locate/jsvi

Investigation of the Causes behind the Vibrations of a High-Speed Solid-Rotor Induction Motor

Sabin Sathyan[a], Anouar Belahcen[a,b], Antti Lehikoinen[a], Ugur Aydin[a], Fredrik Boxberg[c]

[a]*Aalto University, Dept. of Electrical Engineering and Automation, PO Box 15500, FI-00076, Finland*
[b]*Tallinn University of Technology Dept. of Electrical Power Engineering and Mechatronics, 19086 Tallinn, Estonia*
[c]*Ingersoll Rand Finland Oy, Metsänneidonkuja 4, 02130 Espoo, Finland*

ARTICLE INFO

Article history:
Received
Received in revised form
Accepted

Keywords:
Finite element analysis
Electrical motors
Magnetomechanical coupling
Vibrations

ABSTRACT

This paper analyzes the causes of vibrations in a solid-rotor induction motor (SRIM) through electromagnetic Finite Element (FE) simulations and laboratory measurements. The computed results are compared with vibration measurements, and the electromagnetic causes of vibrations were discovered, including the fault related reasons. The machine under investigation is a 300 kW, 60 000 rpm, three-phase SRIM for industrial air compression. The FE simulations are carried out in an open source FE library implemented in Matlab. Both magnetic forces and magnetostriction deformations are accounted for in the simulations. This magneto-mechanical coupling is implemented using a free-energy-based model. The harmonic analysis of the vibrations revealed that, the supply frequency components, the magnetic forces and the magnetostriction contribute to the electromagnetic causes of vibration, while there is a significant amount of vibration produced due to the rotor eccentricity in the motor.

1. Introduction

The vibrations in electrical machines cause unwanted noise in neighboring environments and it can also lead to diminished performance and lifespan of machines. Numerical simulations to analyze and predict these vibrations are hence substantial in machine design. In industrial machinery, the noise analysis is a complex procedure, because there are mechanical sources of vibrations apart from electromagnetic reasons, and interference from nearby electrical and mechanical installations makes the situation more

* *Corresponding author.* Tel.: +358-4066-28668
E-mail address: sabin.sathyan@aalto.fi
Peer review under responsibility xxx

http://dx.doi.org/

challenging.

This study examines the topic of vibration analysis predominantly from an electromagnetic standpoint and correlated the findings with unbalances in the motor system. The study of vibrations and noise has been a prominent topic in electrical machines and electromechanics for decades. Magnetic forces and magnetostriction (MS) were found to be the major electromagnetic causes of vibration [1]. The severity of these two phenomena depends on factors including the manner of machine excitation, type of the machine and design parameters, for instance number of poles, airgap length, winding configuration and type of materials used. The factors that make this study exclusive in magneto-mechanical analysis of high-speed motors are; a comprehensive examination of electromagnetic factors such as electromagnetic stress and MS has been done, including the contribution of eccentricity in motor vibrations using an all-encompassing analytical model and comparison between analytical results, simulations and measurements. Furthermore, combined FE and measurement-based magneto-mechanical vibration analysis of solid-rotor high speed motor for industrial applications is an originality element of this work.

The use of solid rotor instead of cage rotor is usually employed for attaining the highest speed of induction motors [2-4]. Also, solid-rotor motors can achieve steady-state stability and linearity of torque-speed characteristics during the course of the whole speed range and has high mechanical integrity and durability. The studies by Huppunen et al. [5] and Gieras et al. [6] on high-speed induction motor proves these characteristics of SRIM. In this paper, the magnetic forces are computed using the Maxwell stress tensor, based on the research by Arkkio [7] and the MS is taken into account in the magneto-mechanical coupled model by making use of Helmholtz free energy density. An extensive study on the free-energy based magnetomechanical model is presented by Fonteyn et al. [8] and Aydin et al. [9,10]. The measurement of vibrations was done in the industrial installation site of the motor.

The presence of rotor eccentricity has been found to be a contributing factor in motor vibrations in previous studies and the same is proved in this paper with the theoretical explanations and measurement results showing eccentricity-induced frequency components. Dorrel et al. [11, 12] examined the unbalanced magnetic pull in motors due to rotor eccentricity. Rodriguez et. al investigated the vibrations occurred in an induction motor using the Maxwell stress tensor method and formulated the system behavior under dynamic eccentricity [13]. The studies and experiments by Hamzaoui et al. shown in [14, 15] explain how the imbalance and misalignment defects can contribute to the vibro-acoustic behavior of electrical motors. They experimentally and theoretically proved how the noise and vibrations are higher in motors with defects compared to those without defects. Han et al. [16] studied the radial and tangential forces caused by rotor eccentricity and proposed a magnetic equivalent circuit model. There are different studies done in the past related to motor faults, in terms of the methods for detection of faults and considerations in motor design accounting for vibrations [17-19]. A detailed study on the FE modelling of the vibro-acoustics behavior of induction motors can be seen in the research of Wang et al. [20]. Recent studies by Lin et al. propose some methods for reducing the vibration and acoustic noise in electrical motors by optimizing magnetic forces [21]. Inspired from the previous researches and the methodologies we have developed, this paper addresses the vibration problem in a high-speed induction motor with an extensive outlook on magnetic forces, magnetostriction and eccentricity.

2. Computational Methodology

2.1. Solving Magnetic Field and Magnetic Forces using FEA

The Maxwell equations of the magnetic field problem are solved numerically using 2D FEA. The magnetic field in the machine core is assumed as two-dimensional and the three-dimensional end regions of the stator are modelled by using constant end-winding impedances in the winding circuit equations. Both the stator and rotor core are modeled as non-linear anhysteretic materials, where the stator is electrically non-conducting, due to thin lamination, and the rotor is conducting. Practically, the time variation of the magnetic field in an electric motor is not sinusoidal and hence, to solve the magnetic field accurately, time-stepping method is required.

The induction motor is considered as a quasi-static magnetic system where the Maxwell field equation can be written as follows:

$$\nabla \times \boldsymbol{E} = -\frac{\partial \boldsymbol{B}}{\partial t} \tag{1}$$

$$\nabla \times \boldsymbol{H} = \boldsymbol{J} \tag{2}$$

$$\boldsymbol{H} = \nu \boldsymbol{B} \tag{3}$$

$$\boldsymbol{J} = \sigma_e \boldsymbol{E} \tag{4}$$

where $\boldsymbol{E}$ is the electric field strength, $\boldsymbol{B}$ is the magnetic flux density, $\boldsymbol{H}$ is the magnetic field strength and $\boldsymbol{J}$ is the current density. The magnetic reluctivity is ν and σ_e is the electric conductivity of the material.

The vector potential formulation was used for the magnetic model, with the governing equation

$$\nabla \times (\nu \nabla \times \boldsymbol{A}) + \sigma_e \frac{d}{dt} \boldsymbol{A} + \sigma_e \nabla V = 0 \tag{5}$$

where $\boldsymbol{A}$ is the vector potential, σ_e is the electrical conductivity, and V is the electric scalar potential for the winding domains. Coupling with the stator and rotor circuit equations was established using the Tsukerman formulation [25]. The electric conductivity of the iron core is set to zero in the simulations, due to the fact that it is made of thin lamina.

The elastic model is represented as

$$\nabla \cdot \sigma(\varepsilon, \boldsymbol{B}) = \rho \frac{d^2}{dt^2} \boldsymbol{u} \tag{6}$$

where σ is the stress sensor, ρ is material density and, $\boldsymbol{u}$ is the vector of displacements. The linear strain is denoted by ϵ

$$\varepsilon = 1/2(\nabla \boldsymbol{u} + \nabla \boldsymbol{u}^T) \tag{7}$$

For the non-linear strain tensor, the invariant model of [9-10] explained in section 2.2 was used, enabling the inclusion of both Maxwell stress and magnetostriction. To obtain a first-order system, the auxiliary variable $v = \frac{d}{dt} u$ was defined. The mechanical equation is solved in solid parts only, whereas the magnetic equation is solved in the whole cross-section including the air regions.

The entire solver was developed by the authors in Matlab, based on the open-source SMEKLib library [23]. As the formulation described yields a non-degenerate non-linear problem (assuming typical boundary conditions), it is straightforward to solve with the Newton-Raphson method. The details on computing the Jacobian matrix can be found in [26].

Maxwell stress tensor method gives the magnetic torque exerted on a ferromagnetic region by integrating on a closed area around the region.

$$T_{em} = \oint_S \boldsymbol{r} \times (\boldsymbol{\tau} \cdot \boldsymbol{n})\, dS = \oint_S \boldsymbol{r} \times \left\{ \frac{1}{\mu_0} (\boldsymbol{B} \cdot \boldsymbol{n}) \boldsymbol{B} - \frac{1}{2\mu_0} \boldsymbol{B}^2 \boldsymbol{n} \right\} dS \tag{8}$$

where $\boldsymbol{\tau}$ is the Maxwell stress tensor, $\boldsymbol{r}$ is a vector representing rotor radius, μ_0 is the permeability of vacuum and $\boldsymbol{n}$ is the normal unit vector of the integration surface dS.

The magnetic force can be calculated from the Maxwell stress tensor by the volume integral $\int_V \nabla . \boldsymbol{\tau} dV$. This volume integral can be reduced to the closed surface integral over a surface S and the force formula becomes

$$F = \oint_S \left(\frac{1}{\mu_0} (B_n \boldsymbol{B} - \frac{1}{2\mu_0} \boldsymbol{B}^2 \boldsymbol{n} \right) dS = \oint_S \left(\frac{1}{2\mu_0} (B_n{}^2 - B_t{}^2) \boldsymbol{n} + \frac{1}{\mu_0} B_n B_t \boldsymbol{t} \right) dS \tag{9}$$

where $\boldsymbol{n}$ and $\boldsymbol{t}$ represent the outward unit vector normal and tangential respectively to the differential surface S.

The quantities inside Eq. (9) can be separated into normal component of traction (σ_r) and circumferential component of traction (σ_ϕ).

$$\sigma_r = \frac{1}{2\mu_0} (B_r{}^2 - B_\phi{}^2) \tag{10}$$

$$\sigma_\phi = \frac{1}{\mu_0}(B_r B_\phi) \tag{11}$$

In order to analyze the spatial distribution and time dependence of the radial stress, it can be developed into two-dimensional Fourier series [1]

$$\sigma_r = \sum_{m=0}^{\infty}\sum_{n=0}^{\infty}\lambda_{mn}\begin{bmatrix} a_{mn}\cos(mp\phi)\cos(n\omega t)+ \\ b_{mn}\cos(mp\phi)\sin(n\omega t)+ \\ c_{mn}\sin(mp\phi)\cos(n\omega t)+ \\ d_{mn}\sin(mp\phi)\sin(n\omega t) \end{bmatrix} \tag{12}$$

where m and n represent the space and time harmonic numbers, p is the number of pole pairs of the machine, ω is the rotational speed (rad/s) of the magnetic field, t and ϕ are the time and angular position respectively. The other constants are calculated as

$$a_{mn} = \frac{p\omega}{2\pi^2\mu_0 r^2}\int_0^{\frac{2\pi}{p}}\int_0^{\frac{2\pi}{\omega}}\sigma_r\cos(mp\phi)\cos(n\omega t)\,d\phi\,dt \tag{13}$$

$$b_{mn} = \frac{p\omega}{2\pi^2\mu_0 r^2}\int_0^{\frac{2\pi}{p}}\int_0^{\frac{2\pi}{\omega}}\sigma_r\cos(mp\phi)\sin(n\omega t)\,d\phi\,dt \tag{14}$$

$$c_{mn} = \frac{p\omega}{2\pi^2\mu_0 r^2}\int_0^{\frac{2\pi}{p}}\int_0^{\frac{2\pi}{\omega}}\sigma_r\sin(mp\phi)\cos(n\omega t)\,d\phi\,dt \tag{15}$$

$$d_{mn} = \frac{p\omega}{2\pi^2\mu_0 r^2}\int_0^{\frac{2\pi}{p}}\int_0^{\frac{2\pi}{\omega}}\sigma_r\sin(mp\phi)\sin(n\omega t)\,d\phi\,dt \tag{16}$$

$$\lambda_{mn} = \begin{cases} (1/4) \text{ for } m=n=0 \\ (1/2) \text{ for } m=0,\ n>0 \text{ and } m>0,\ n=0 \\ 1 \text{ for } m>0,\ n>0 \end{cases} \tag{17}$$

The spatial order m represents the mode shape of the vibration, while the time order n determines the corresponding vibration frequency. The radial stress calculated using Eq. (12) can be represented as a sum of waves circulating clockwise and anticlockwise direction with respect to the rotational direction of the motor. Then the radial stress can be written as

$$\sigma_r = \sum_{m=0}^{\infty}\sum_{n=0}^{\infty}\begin{bmatrix} \frac{1}{2}\lambda_{mn}\left\{(a_{mn}+d_{mn})^2+(b_{mn}-c_{mn})^2\right\}^{\frac{1}{2}} \\ \cos(-mp\phi+n\omega t+\gamma_{+})+ \\ \frac{1}{2}\lambda_{mn}\left\{(a_{mn}-d_{mn})^2+(b_{mn}+c_{mn})^2\right\}^{\frac{1}{2}} \\ \cos(mp\phi+n\omega t+\gamma_{-}) \end{bmatrix} \tag{18}$$

The presence of an unbalance in the form of static or dynamic rotor eccentricity in the motor can produce additional force components in stress distribution [17]. The dynamic eccentricity is illustrated in Fig. 1. If there is no eccentricity and the stator and rotor are concentric, the resultant radial force acting between the two cylindrical bodies is zero. The rotor eccentricity creates an unbalanced magnetic pull [11] that even pulls the rotor further from the concentric position.

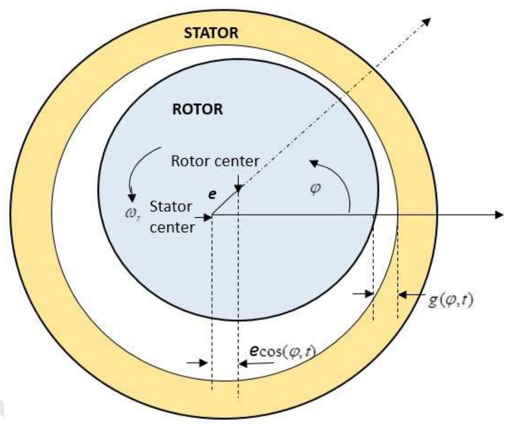

Fig. 1. Illustration of dynamic eccentricity in a motor

For a motor with dynamic eccentricity, the airgap length is no longer constant and can be expressed as [12, 13],

$$g(\varphi,t) = g[1-d_e\cos(2\pi f_r-\varphi)] \tag{19}$$

where g is the average airgap length, φ is the angular position along the airgap, d_e is the degree of dynamic eccentricity and f_r is the rotor rotational frequency. For small values of dynamic eccentricity, the airgap permeance Λ can be represented as [12],

$$\Lambda(\varphi,t) = \frac{1}{g}[1+d_e\cos(2\pi f_r-\varphi)] \tag{20}$$

There is magnetic flux passing through the airgap even with the dynamic eccentricity. With this assumption, the magnetic flux can be expressed as

$$b(\varphi,t)=\Lambda(\varphi,t)\int \mu_0 j_S(\varphi,t)d\varphi \qquad (21)$$

where j_s is the stator current density given by

$$j_S(\varphi,t)=J\sin(2\pi f_S t-p\varphi) \qquad (22)$$

where f_s is the fundamental supply frequency. Substituting (20) and (22) in (21) gives

$$\begin{aligned}b(\varphi,t)&=B_S{}^{p}\cos(2\pi f_S t-p\varphi)+B_S{}^{p-1}\cos[(2\pi f_S-2\pi f_r)t-(p-1)\varphi]\\&+B_S{}^{p+1}\cos[(2\pi f_S+2\pi f_r)t-(p+1)\varphi]\end{aligned} \qquad (23)$$

$$\text{where } B_S{}^{p}=\frac{\mu_0 J_S}{pg};\qquad B_S{}^{p\pm 1}=\frac{\mu_0 J_S}{2pg}d_e \qquad (24)$$

The radial force per unit area can be expressed as

$$F(\varphi,t)=\frac{1}{2\mu_0}b^2(\varphi,t) \qquad (25)$$

Replacing (23) in (25) gives

$$F(\varphi,t)=\frac{1}{2\mu_0}\{(B_S{}^{p})^2\cos(4\pi f_S t+2p\varphi) \qquad (26a)$$

$$+B_S{}^{p-1}B_S{}^{p+1}\cos(4\pi f_r t-2\varphi) \qquad (26b)$$

$$+B_S{}^{p}B_S{}^{p-1}\cos(2\pi f_r t+2p\varphi) \qquad (26c)$$

$$+B_S{}^{p-1}B_S{}^{p}\cos[(4\pi f_S+2\pi f_r)t-\varphi] \qquad (26d)$$

$$+B_S{}^{p+1}\cos[(4\pi f_S-2\pi f_r)t-\varphi]\} \qquad (26e)$$

$$+\left(B_S{}^{p+1}\right)^2\cos[2(2\pi f_S+2\pi f_r)t-2(p+1)\varphi] \qquad (26f)$$

$$+\left(B_S{}^{p-1}\right)^2\cos[2(2\pi f_S-2\pi f_r)t-2(p-1)\varphi] \qquad (26g)$$

The equation (26) represents the frequency components when dynamic eccentricity is present. Dynamic eccentricity may produce other vibrations than twice-supply frequency $2f_S$ (26a), in addition to the rotational frequency f_r . Those components are $2f_r$ (26b) which is twice the rotor frequency, $2f_s \pm f_r$ presented in (26d) and (26e), $2(f_s \pm f_r)$ as shown in (26f) and (26g). To generalize the frequency components in terms of the multiples of the supply frequency, the additional frequency components can be quantified as $2f_{r,k}$, $2f_{s,k} \pm f_r$ and $2(f_{s,k} \pm f_r)$ where k is an integer. These frequency components are affected by the slip and hence an additional +/- sf_s term will be reflected in these frequencies.

The radial stress shown in equation (18) can be written as

$$\sigma_r = \sum_{m=0}^{\infty} \sum_{n=0}^{\infty} \lambda_{mn} \cos(mp\phi \pm n\omega t + \varphi_{m,n}) \tag{27}$$

Due to the presence of dynamic eccentricity, the airgap permeance will have an additional term $\Lambda_{rd} = \frac{g}{e_d}\cos(\phi - \omega t - \alpha_d)$ where α_d is the original position of the eccentricity. The radial airgap flux density is

$$B_r = \varepsilon_m \cdot (\Lambda + \Lambda_{rd}) = \varepsilon_0 \cos(p(\phi - \omega t) - \varphi) \cdot \frac{\mu_0}{e}[1 + \frac{g}{e_d}\cos(\phi - \omega t - \alpha_d)] \tag{28}$$

where $e_d = e\cos(\omega t)$, ε_m is the m.m.f produced by the stator and rotor windings, ε_0 is the amplitude of the m.m.f. The equation (28) can be further developed as

$$B_r = B_0 \cos(p(\phi - \omega t) - \varphi) + B_e \cos[(p \pm 1)(\phi - \omega t) - (\varphi \pm \alpha_d)] \tag{29}$$

where $B_e = B_0 \times \frac{g}{2e_d}$ is the amplitude of eccentric magnetic flus density and $B_0 = \frac{\varepsilon_0 \mu_0}{g}$ is the amplitude of the original flux density.

Now, from the relation $\sigma_r = B^2{}_r / 2\mu_0$, the stress can be written as

$$\begin{aligned}\sigma_r = [&B_0^2 \cos(2p(\phi - \omega t) - 2\varphi) \\ &+ B_e^2 \cos(2(p \pm 1)(\phi - \omega t) - 2(\varphi \pm \alpha_d)) \\ &+ 4B_0 B_e \cos((2p \pm 1)((\phi - \omega t) - 2(\varphi \pm \alpha_d)) \\ &+ 4B_0 B_e \cos(\pm(\phi - \omega t) - 2(\varphi \pm \alpha_d))] 4\mu_0\end{aligned} \tag{30}$$

Hence, without any eccentricity, there is only a stress wave rotating at $n\omega = 2p\omega$ speed and with a spatial order of m = 2p. In the presence of an eccentricity, new spatiotemporal waves occurs and these terms are modulations at $2(p \pm 1)$, $2p \pm 1$ and ± 1 of the spatiotemporal waves. Therefore, dynamic eccentricities in a motor will produce modulations of the magnetic forces that are non-multiples of the number of pole pair.

From the abovementioned analytical model, it can be concluded that the dynamic eccentricity produces additional force frequencies and subsequently the stator deformation and vibration will have the same frequency components, due to its linear mechanical behaviour. The analytical model explains how the different frequencies are originated under a dynamic eccentricity and this model is not used in the simulations. However, the simulated frequencies agree with the analytical ones given in the results section.

2.2. Energy based Magnetomechanical Model

In order to couple the magnetic and elastic properties of the material, the constitutive equations are formulated from a Helmholtz free energy density ψ [8-10]. For an isotropic magneto-elastic material, ψ is expressed as a function of five scalar invariants, which depend on the magnetic flux density vector $\boldsymbol{B}$ and the total strain tensor $\boldsymbol{\varepsilon}$:

$$I_1 = \mathrm{tr}(\boldsymbol{\varepsilon}), \quad I_2 = \frac{1}{2}\mathrm{tr}(\boldsymbol{\varepsilon}^2), \quad I_4 = \frac{\boldsymbol{B}\cdot\boldsymbol{B}}{\boldsymbol{B}_{ref}^2}, \quad I_5 = \frac{\boldsymbol{B}\cdot(\tilde{\boldsymbol{\varepsilon}}\boldsymbol{B})}{\boldsymbol{B}_{ref}^2}, \quad I_6 = \frac{\boldsymbol{B}\cdot(\tilde{\boldsymbol{\varepsilon}}^2\boldsymbol{B})}{\boldsymbol{B}_{ref}^2} \tag{31}$$

where $\boldsymbol{B}_{\mathrm{ref}}$ = 1 T. The first three invariants describe the elastic behavior of the material, and I_3 (not defined here) is not used, as linear elasticity is assumed. The fourth invariant corresponds to the single-valued magnetization behavior and the fifth and sixth invariants determine the magneto-elastic coupling. Since the permeability variation is independent of the hydrostatic pressure, in the fifth and sixth invariants, the deviatoric part of the strain $\tilde{\varepsilon} = \varepsilon - \varepsilon_{Hyd}$ is used, where ε_{Hyd} is the hydrostatic strain. The expression for the Helmholtz free energy density is then given as

$$\psi = \frac{1}{2}\lambda I_1^2 + 2GI_2 - \nu_0\left(\frac{I_4}{2} + \sum_{i=0}^{n_\alpha-1}\frac{\alpha_i}{i+1}I_4^{i+1} + \sum_{i=0}^{n_\beta-1}\frac{\beta_i}{i+1}I_5^{i+1} + \sum_{i=0}^{n_\gamma-1}\frac{\gamma_i}{i+1}I_6^{i+1}\right) \tag{32}$$

Here λ and G are the Lamé constants of the material, ν_0 is the reluctivity of free space and α_i, β_i, γ_i are the fitting parameters to be identified from measurements. The magneto-elastic stress and magnetization are obtained as

$$\boldsymbol{\sigma}_{me}(\boldsymbol{B},\boldsymbol{\varepsilon}) = \frac{\partial\psi(\boldsymbol{B},\boldsymbol{\varepsilon})}{\partial\boldsymbol{\varepsilon}} \quad \text{and} \quad \boldsymbol{M}(\boldsymbol{B},\boldsymbol{\varepsilon}) = -\frac{\partial\psi(\boldsymbol{B},\boldsymbol{\varepsilon})}{\partial\boldsymbol{B}} \tag{33}$$

The magnetic field strength vector is then computed as $\boldsymbol{H} = \nu_0\boldsymbol{B} - \boldsymbol{M}$. The magneto-elastic stress tensor $\boldsymbol{\sigma}_{me}$ consists of elastic and MS related stress tensors.

Fifteen parameters were needed to model the properties of the studied material (0.5 mm non-oriented Fe-Si electrical sheets) and they were determined using the experimental data obtained from a custom-built uniaxial single sheet tester [22]. In the experimental process, the material was loaded with different stresses varying from 50 MPa compression (−) to 80 MPa tension (+) parallel to the flux density, and the magnetization curves were measured. Afterward, the initial fitting of the single-valued model parameters to the ***H***-averaged measured magnetization curves was realized at various stress values, as shown in Fig. 2. Magnetic materials show reduced permeability under compression and high tension. This behaviour of magnetic materials is modelled successfully using the model. Besides, increased permeability is observed under low tensile stress as reported in [22]. It is worth mentioning that, although the material model is identified only by using the uniaxial stress dependent *B*-*H* curves, it is able to predict the magnetic behaviour of the material under multi-axial stress [10].

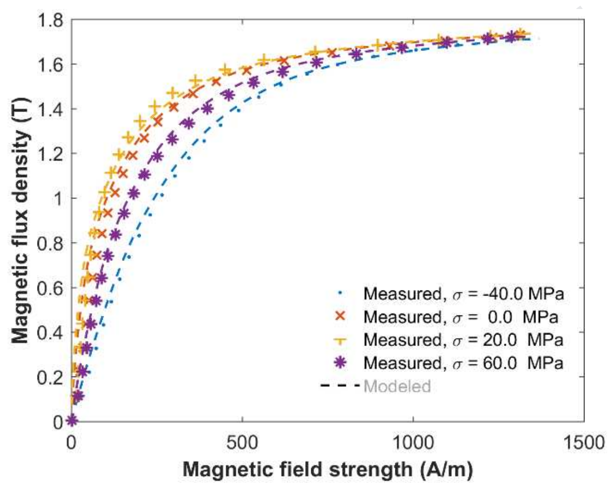

Fig. 2. Fitting results of the single-valued model parameters with ***H***-averaged magnetization curve measurements [10]

3. Vibration Measurements

3.1. Accelerations Measurement

The specifications of the solid rotor motor under investigation are given in Table I. For measuring the acceleration, eight tri-axial accelerometers of Brüel&Kjær type 4524B were used simultaneously and the PULSE analyzer used was multi-axial Brüel&Kjær LAN-XI type 3050-A-060, which is a real-time, multi-channel sound and vibration data acquisition system. The accelerometers were attached at eight different positions on the air compressor installation to measure the vibrations produced by the motor and other equipments. A schematic diagram showing the placement of accelerometers around the motor structure is given in Fig. 3. Two accelerometers were attached on the top of the compressor body in bearing planes (numbered 1 and 2 in fig. 3), four were exactly next to the fitting points of the motor (number 3 , 4, 5 and 6), and one in the inlet duct of cooling air (number 7) and the final one in the outlet duct (number 8). The acceleration was measured in all the three directions, X-vertical, Y-horizontal, and Z-axial.

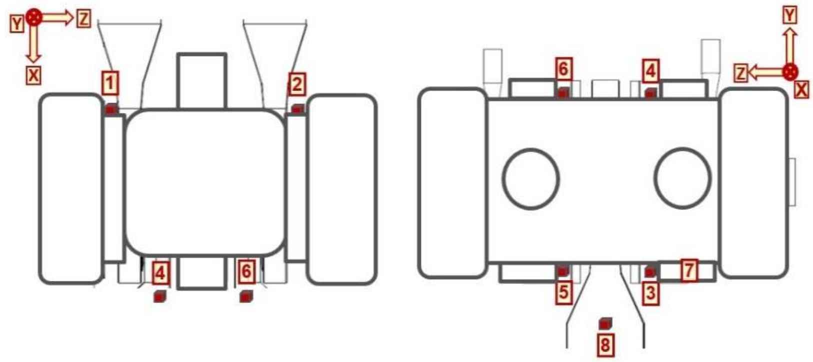

Fig. 3. Schematic diagram showing the position of accelerometers around the motor structure

Table 1.
Specifications of the Solid-rotor Induction Motor

Specifications	Unit	Value
Power	kW	300
Voltage (line-to-line)	V	400
Rated speed	rpm	60 000
Number of poles		2
Stator outer diameter	mm	250
Stator inner diameter	mm	116

4. Results and Discussion

In this section, the measurement results are explained in the beginning and later, the simulation results and the comparison of those with the measurements are explained.

4.1 Measured Vibration Spectra

The Fourier analysis of vibrations gives the frequency components present in them. Fig. 4 and Fig. 5 show the frequency components in the measured accelerations at sensor 1, in radial and tangential direction respectively. The radial plots are given in black color and the tangential ones in blue. There are higher values of acceleration components at frequencies 1000 Hz, 2000 Hz, 3000 Hz, 4000 Hz, 5000 Hz, 6000 Hz and 7000 Hz. The detailed analysis of these frequencies and sidebands are given in section 4.3.

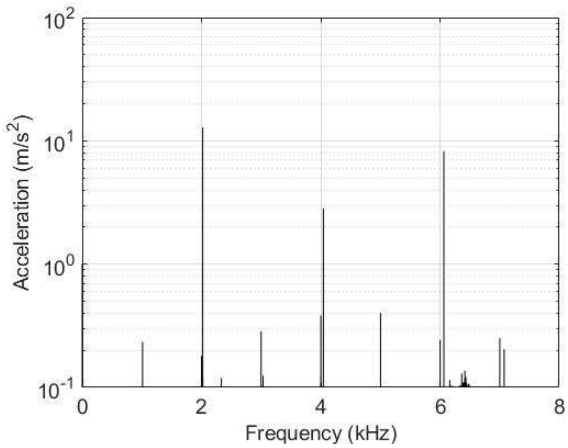

Fig. 4. Frequency spectrum of measured radial accelerations at a motor speed of 60000 rpm, with a motor load of 51 Nm.

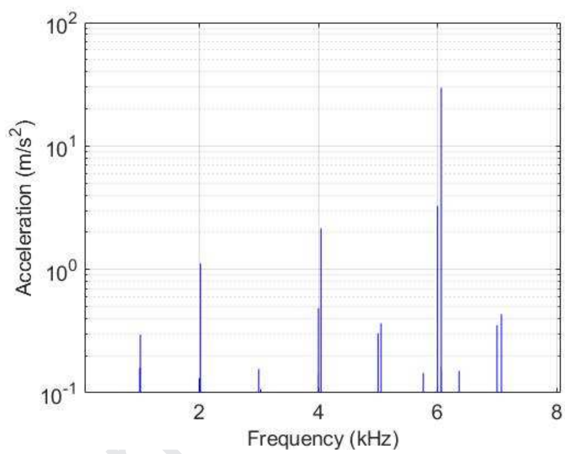

Fig. 5. Frequency spectrum of measured tangential accelerations at a motor speed of 60000 rpm, with a motor load of 51 Nm.

4.2 Simulation Results of Magnetomechanical Model

The energy-based magneto-mechanical model is used for simulating the motor in Matlab. The magneto-mechanical model based on free energy principle was simulated with PWM supply having one pulse per half period, as in the original measurement source. The results shown are from time-stepping simulations with simulation time 0.015 s and has a time step length of 5e^{-6} s. The number of elements were 2976. The second order mesh of the simulated motor is given in Fig. 6 and the flux density distribution is shown in Fig. 7. The magnetomechanical problem was solved with the finite element method implemented in Matlab using an open-source library [23]. For this purpose, second-order shape functions were used for both the vector potential and the displacements. All field and windings circuit quantities were strongly coupled. The rotation of the rotor was considered with the moving band approach [24], and the same air-gap mesh was used to evaluate the weighted Maxwell stress tensor in the air-gap.

In the radial displacement simulation, the displacement of the outer nodes of the stator and inner nodes of the rotor were fixed to zero in tangential direction. The same were fixed in radial direction for the tangential displacement simulations. The displacement at a point on the stator surface due to magnetic forces and MS are given in Fig. 8. In Fig. 9, simulated displacement in three cases are given. The displacement due to magnetic forces and due to MS are in phase and they get added up. Hence the final displacement increases with the interaction of magnetic forces and MS in the case of the studied motor. The Fourier analysis of the radial displacements, showing the frequency components are given in Fig. 10 for normal operation and in Fig. 11 with a dynamic eccentricity of 14%. The introduction of dynamic eccentricity has produced additional components in the frequency spectrum.

In the simulated spectrum, there are high magnitude of displacement at frequencies 1000 Hz, 2000 Hz, 3000 Hz, 4000 Hz, 5000 Hz and 6000 Hz. It must be noted that, the aim of this study is not to determine the amplitude of the induced deformation or vibration, but to find out the frequency components present in them and to examine how they originated. This information also helps to analyze the contribution of faults such as eccentricity in motor vibrations. The amplitude of the deformations and vibrations vary with the type of motor (the size and power) and its load conditions [19]. The simulated tangential displacements are shown in Fig. 12.

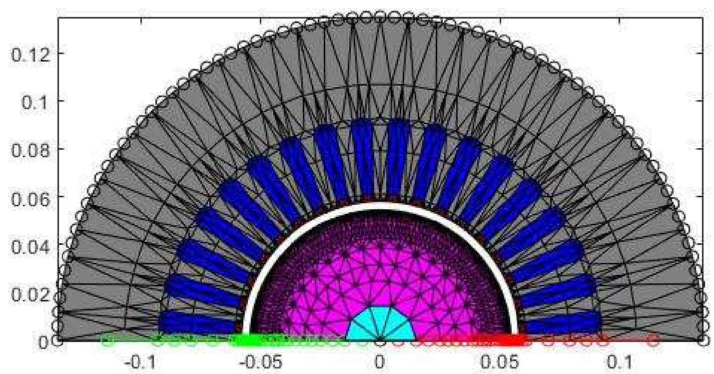

Fig. 6. The finite element mesh of the simulated motor in Matlab

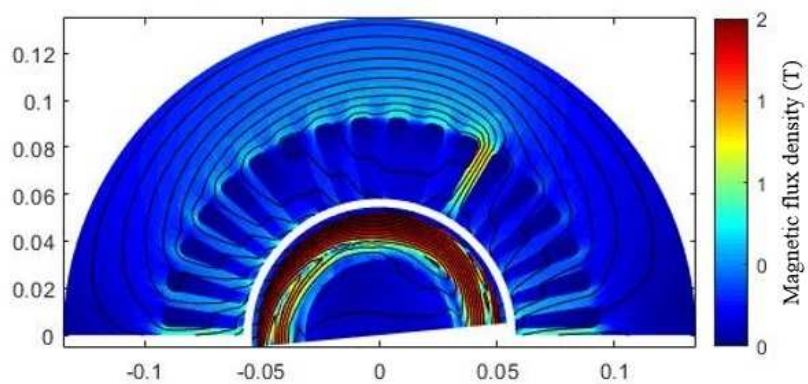

Fig. 7. Magnetic flux density distribution in the motor cross section

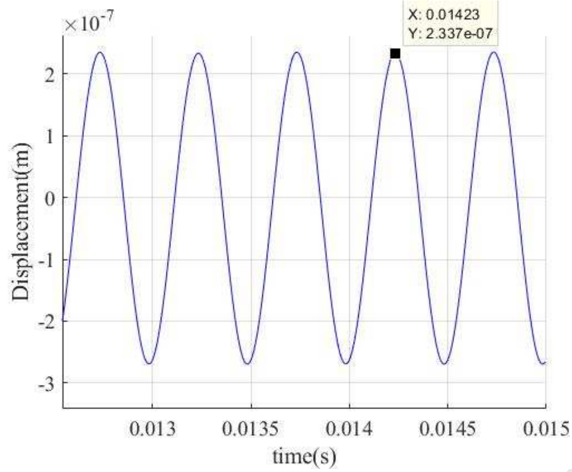

Fig. 8. Simulated displacement due to magnetic forces and MS, at a point on the stator outer surface

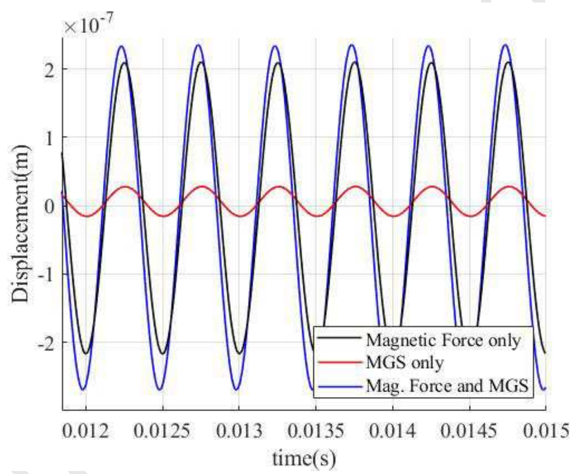

Fig. 9. Simulated displacement at a point on the stator outer surface of the motor

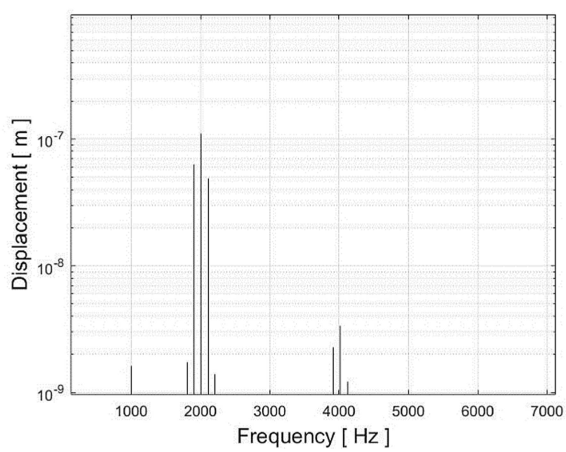

Fig. 10. Frequency spectrum of the simulated radial displacement under normal operation

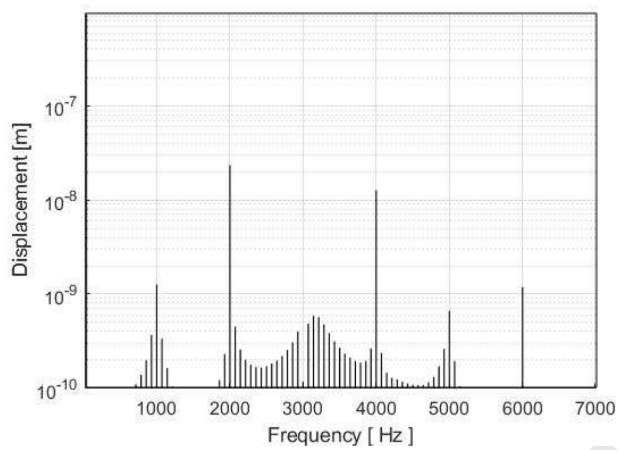

Fig. 11. Frequency spectrum of the simulated radial displacement when the motor has dynamic eccentricity

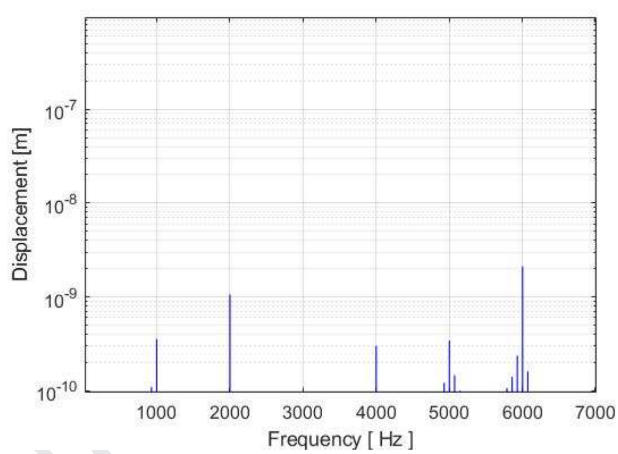

Fig. 12. Frequency spectrum of the simulated tangential displacement when the motor has dynamic eccentricity

4.3 Analysis of Frequency Components and Sidebands

The theoretical study on magnetic forces and the frequency components contributed by dynamic eccentricity are discussed in section II. A. The rotor rotational frequency f_r is 1000 Hz, supply frequency f_s is 1008.75 Hz and the slip is 0.00875. The Fig. 13 shows the measurement results of the major radial acceleration amplitudes above 1 m/s^2 around 2000 Hz, 4000 Hz and 6000 Hz frequencies. In Table 2, the origination of different frequency components from the measurement shown in Fig. 13 are detailed.

In Fig. 14, the frequency components in the tangential acceleration are shown. The acceleration corresponds to a displacement d and angular frequency $\omega = 2\pi f$ can be calculated by the formula $\omega^2 d$. For example, the amplitude of radial acceleration from measurement is 12 m/s^2 at 2017 Hz. In the simulation, the computed displacement was 2.3 e-8 m at 2017 Hz. The acceleration from this displacement is calculated as 3.7 m/s^2. In the simulation, the rigid body motion and the frame of the motor is not modelled, and hence the simulated acceleration will not have the effect of frame. This is the reason behind the difference in the amplitude between measured and simulated accelerations. The measurement data can also be influenced by the damping and resonance of the housing and support structures of the motor.

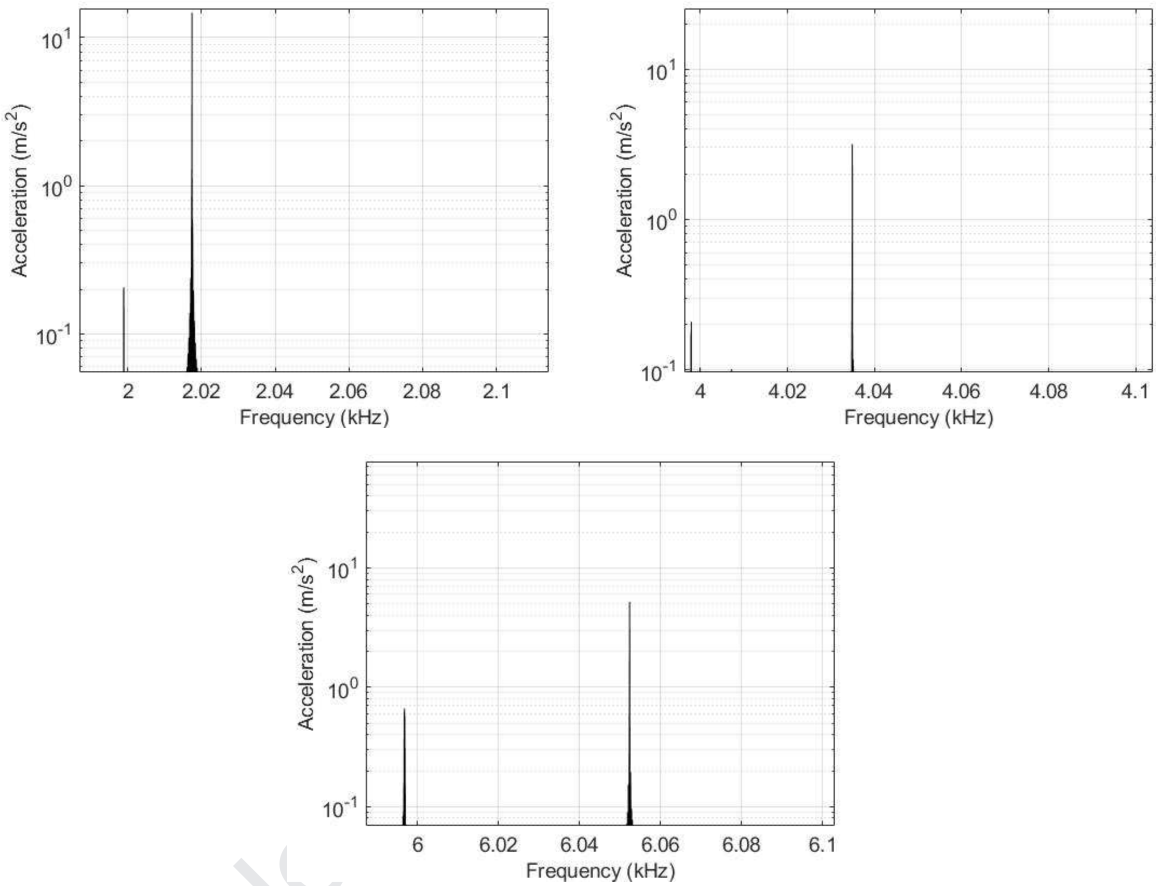

Fig. 13. Frequency spectrum of measured radial acceleration showing 2017 Hz, 4035 Hz and 6052 Hz and their sidebands 1999 Hz, 3999 Hz and 5999 Hz respectively

Table 2.
Origination of frequency components in the spectrum of radial acceleration

Frequency	**Value (Hz)**	**Sideband**	**Value (Hz)**
$\mathbf{f_s}$	**1008.75**		
$\mathbf{2f_s}$	**2017.5**	$\mathbf{2(f_s\text{-}sf_s)}$	2*(1008.75-(1008.75*0.00875)=**1999**
$\mathbf{2p*2f_s}$	(2*1)*2017.5=**4035**	$\mathbf{2p*2(f_s\text{-}sf_s)}$	2*(1008.75-(1008.75*0.00875)=**3998**
$\mathbf{(2p+1)*2f_s}$	(2+1)*2017.5=**6052**	$\mathbf{(2p+1)*2(f_s\text{-}sf_s)}$	3*2*(1008.75-(1008.75*0.00875)=**5999**
$\mathbf{2f_{s,k}+f_r}$ **; k=1**	(2*1008.75)+1000=3017.5	**2fs,k+fr +sfs**	(2*1008.75)+1000+ (1008.75*0.00875) = **3026**
$\mathbf{2f_{s,k}+f_r}$ **; k=2**	(2*2*1008.75)+1000=5035	**2fs,k+fr + sfs**	(2*2*1008.75)+1000+ (1008.75*0.00875) =**5043**

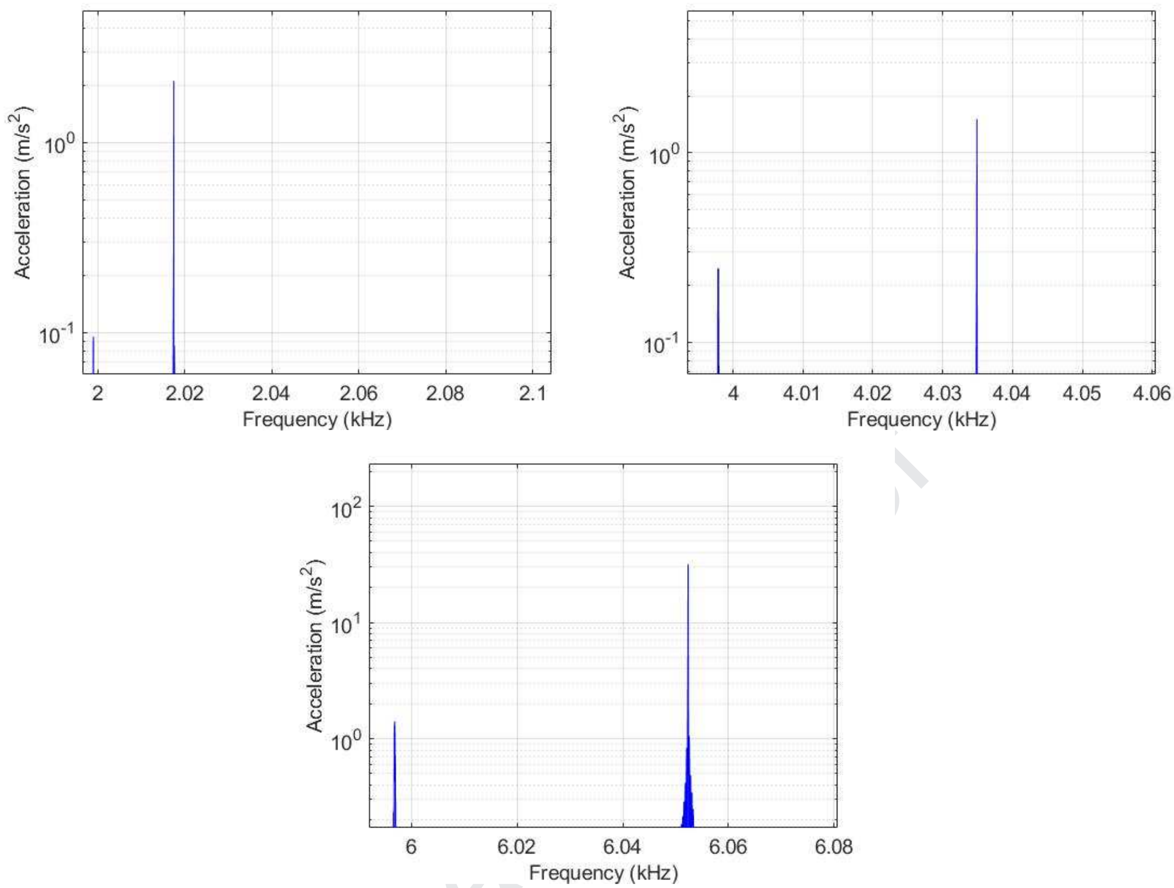

Fig. 14. Frequency spectrum of measured tangential acceleration showing 2017 Hz, 4035 Hz and 6052 Hz and their sidebands 1999 Hz, 3999 Hz and 5999 Hz respectively

In Fig. 15, simulated results of the major radial frequency components at 2017 Hz, 4035 Hz and 6052 Hz are given. It can be seen that the theoretically proven components are present in this simulated spectra at the same frequencies like in the measurement as shown in Fig. 13. The same results were achieved for tangential frequency spectra also. Hence, it can be concluded from the simulation and measurement results that, the supply frequency, rotor frequency and the additional components due to dynamic eccentricity are the major contributing factors of the motor deformation and thereby the accelerations.

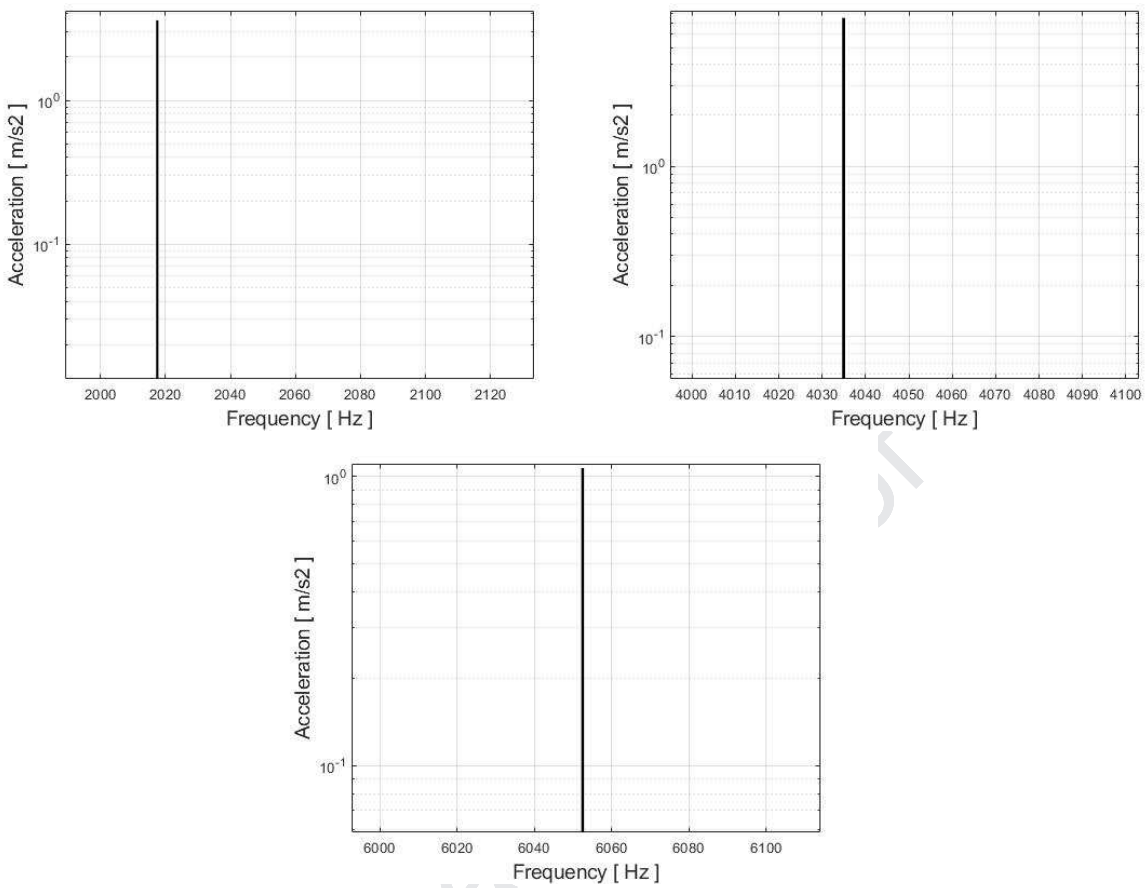

Fig. 15. Frequency spectrum of simulated radial accelerations at 2017 Hz, 4035 Hz and 6052 Hz in the presence of dynamic eccentricity

From the comparative study of measurement and simulated spectra, the frequencies present in both measurement and simulation are matching when a dynamic eccentricity is present in the motor. This is a significant result in terms of condition monitoring, assembling of the motor set-up and acoustic noise problems. The extra frequency components due to eccentricity could contribute to additional acoustic noise. In terms of amplitudes of the acceleration, the simulated spectra show rather similar outputs, although a precise agreement cannot be attained, because the amplitudes can be affected by external factors at the measurement set up and this will not reflect in the simulations. The results point out the presence of dynamic eccentricity in the motor according to this study. This needs to be investigated to find out the root causes of eccentricity that cause the unbalance in the motor system.

5. Conclusion

An extensive study on the electromagnetic causes of vibrations in a high-speed induction motor is carried out for this paper. In the case of the investigated machine, while the fundamental supply frequency components and its multiples cause vibrations, the presence of dynamic eccentricity contribute additional frequency components and hence intensified the vibrations. The frequency components and their sidebands induced by the eccentricity condition were found to be the same in both simulated and measured spectra. The contribution of dynamic eccentricity to the frequency spectra of vibrations is explained and verified with detailed analytical models with measurement verification. Besides, it has been inferred that, magnetostriction is a factor that needs be considered in vibration studies, since the interaction of magnetic forces and magnetostriction could cause changes in magnitudes of the stator vibrations. In the context of the sound and vibration studies in industrial environments, this study provides a vital perspective on the importance of electromagnetic analysis of electrical machines. Because, the results of this work imply that the root causes of the sound or acoustic noise emitting from an electrical motor system can be from the active parts of the motor itself and those areas need to be investigated before going for more mechanical and aerodynamic facets of the machine set-up. The future part of this study will be Boundary Element Method (BEM) based acoustic noise analysis, and to analyze the aeroacoustics effects in noise production.

Acknowledgments

The first author thanks Ingersoll Rand Oy, Finland for their financial support.

References

[1] A. Belahcen, Magnetoelasticity, magnetic forces and MS in electrical machines, doctoral thesis, Helsinki University of Technology, Lab. of Electromechanics, report. 72, pp 23-32, 2004.
[2] J. F. Gieras, Solid-rotor induction motors, in Handbook of Electric Motors, G. Kliman, and H. Tolyiat, Eds., 2nd ed. New York: Marcel Dekker, sec. 2.5.5 and 4.6.2, 2004.
[3] W. L. Song, G. B. Kliman, R. N. Johnson, R. A. White, and J. E. Miller, Novel high-speed induction motor for a commercial centrifugal compressor, IEEE Trans. Magn.36 (2000) 706–713. DOI: 10.1109/28.845043.
[4] J. Pyrhonen, J. Nerg, P. Kurronen, and U. Lauber, High-speed high-output solid-rotor induction-motor technology for gas compression, IEEE Trans. Ind. Electron. 57(2010) 272–280. DOI: 10.1109/TIE.2009.2021595.
[5] J. Huppunen, High-speed solid-rotor induction machine-electromagnetic calculation and design, doctoral thesis, Lappeenranta University of technology, ISBN 951-764-981-9, pp 18-21, 2004.
[6] J. F. Gieras and J. Saari, Performance calculation for a high-speed solid-rotor induction motor, IEEE Trans. Ind. Electron.59 (2012) 2689-2700. DOI: 10.1109/TIE.2011.2160516.
[7] A. Arkkio, Analysis of induction motors based on the numerical solution of the magnetic field and circuit equations, doctoral thesis, Acta Polytechnica Scandinavia, Elec. Eng. Series n. 59, p. 55, 1987.
[8] K. Fonteyn, A. Belahcen, R. Kouhia, P. Rasilo, and A. Arkkio, FEM for directly coupled magneto-mechanical phenomena in electrical machines, IEEE Trans. Magn.46 (2010) 2923–2926. doi:10.1109/TMAG.2010.2044148.
[9] U. Aydin, P. Rasilo, D. Singh, A. Lehikoinen, A. Belahcen, A. Arkkio, Coupled magneto-mechanical analysis of iron sheets under biaxial stress, IEEE Trans. Magn.52 (2016) 1-4. doi:10.1109/TMAG.2015.2496207.
[10] U. Aydin, P. Rasilo, F. Martin, D. Singh, L. Daniel, A. Belahcen, R. Kouhia, A. Arkkio, Modelling the effect of multiaxial stress on magnetic hysteresis of electrical steel sheets: a comparison, IEEE Trans. Magn. 53 (2017) 1–4. doi:10.1109/TMAG.2017.2658676.
[11] D. G. Dorrell, The influence of rotor skew on unbalanced magnetic pull in cage induction motors with eccentric rotors, Proc. 7th Int. Conf. Elect. Mach. Drives (1995) 67–71.
[12] D. G. Dorrell, W. T. Thomson, and S. Roach, Analysis of airgap flux, current, and vibration signals as a function of the combination of static and dynamic airgap eccentricity in 3-phase induction motors, IEEE Trans. Ind. Appl.33 (1997) 24–34. DOI: 10.1109/28.567073.
[13] P. V. J. Rodríguez, A. Belahcen, A. Arkkio, A. Laiho, and J. A. Antonino-Daviu, Air-gap force distribution and vibration pattern of Induction motors under dynamic eccentricity, Elect. Eng. 90 (2007) 209–218. doi:10.1007/s00202-007-0066-2.
[14] N. Hamzaoui, C. Boisson, and C. Lesueur, Vibro-acoustic analysis and identification of defects in rotating machinery, Part I: Theoretical model, Journal of Sound and Vibration, 216(4) (1998) 553-570. https://doi.org/10.1006/jsvi.1995.1713.
[15] N. Hamzaoui, C. Boisson, and C. Lesueur, Vibro-acoustic analysis and identification of defects in rotating machinery, Part II: Experimental study", Journal of Sound and Vibration, 216(4) (1998) 571-583. https://doi.org/10.1006/jsvi.1995.1714.
[16] X. Han, A. Palazzolo, Unstable force analysis for induction motor eccentricity, Journal of Sound and Vibration 370 (2016) 230-258. https://doi.org/10.1016/j.jsv.2016.01.045.
[17] Pöyhönen S, Negrea M, Jover P, Arkkio A, Hyötyniemi H, Numerical magnetic field analysis and signal processing for fault diagnostic of electrical machines, COMPEL Int J Comput Math Elect Eng. 22(4) (2003) 969–981.

[18] K. M. Sousa, U. J. Dreyer, C. Martelli, and J. C. C. da Silva, Dynamic eccentricity induced in induction motor detected by optical fiber bragg grating strain sensors, IEEE Sensors journal 16 (2016) 4786–4792. doi:10.1109/JSEN.2016.2554885.

[19] S. P. Verma and R. S. Girgis, Considerations in the choice of main dimensions of stators of electrical machines in relation to their vibration characteristics, IEEE Trans. Power App. Syst. 94 (1975) 2151–2159. DOI: 10.1109/T-PAS.1975.32066.

[20] C. Wang and J.C.S. Lai, Vibration analysis of an induction motor, Journal of Sound and Vibration 224 (1999) 733-756. https://doi.org/10.1006/jsvi.1999.2208.

[21] F. Lin, S.G. Zuo, W. H. Deng, and S.L. Wu, Reduction of vibration and acoustic noise in permanent magnet synchronous motor by optimizing magnetic forces, Journal of Sound and Vibration 429 (2018) 193-205. https://doi.org/10.1016/j.jsv.2018.05.018

[22] D. Singh, P. Rasilo, F. Martin, A. Belahcen, and A. Arkkio, Effect of mechanical stress on excess loss of electrical steel sheets, IEEE Trans. Magn. 51 (2015) 1-4. doi:10.1109/TMAG.2015.2449779.

[23] A. Lehikoinen ,T. Davidsson , A. Arkkio , A. Belahcen, A high-performance open-source finite element analysis library for magnetics in MATLAB, Proceedings of the IEEE XIII International Conference on Electrical Machines (ICEM) (2018) 486-492.

[24] B. Davat, Z. Ren, M. Lajoie-Mazenc, The movement in the field modeling, IEEE Trans. Magn. 21 (1985) 2296-2298. DOI: 10.1109/TMAG.1985.1064185.

[25] Tsukerman, I. A., Konrad, A. and Lavers, J. D., A method for circuit connections in time-dependent eddy current problems, IEEE Transactions on Magnetics 28(2) (1992) 1299–1302. DOI: 10.1109/20.123928.

[26] P. Rasilo, L. Perkkio, A. Hannukainen, B. Silwal, T. Eirola, A. Arkkio, Instantaneous Power Balance in Finite-Element Simulation of Electrical Machines, *IEEE Trans. Magn.* 50 (2014). doi:10.1109/TMAG.2013.2294945.